Article

Composition and morphology tuning during hydrothermal synthesis of $Sr_xBa_{1-x}Nb_2O_6$ tetragonal tungsten bronzes studied by in situ X-ray diffraction

Received 00th January 20xx,
Accepted 00th January 20xx

DOI: 10.1039/x0xx00000x

Ola G. Grendal, [a] Anders B. Blichfeld, [a] Tuong D. Vu, [a] Wouter van Beek, [b] Sverre M. Selbach, [a] Tor Grande [a] and Mari-Ann Einarsrud*[a]

Current interest in 1D ferroelectric materials calls for cheap, controllable, reproducible and environmentally friendly synthesis routes. Hydrothermal synthesis stands out as one of the most promising routes, but a thorough understanding of nucleation and growth mechanisms is needed for full utilization and control. Here we present a new hydrothermal route for preparing $Sr_xBa_{1-x}Nb_2O_6$ (x = 0.32 - 0.82, SBN) tetragonal tungsten bronzes. The nuclation and growth of SBN were studied by a combination of *in situ* synchrotron X-ray diffraction and *ex situ* scanning electron microscopy (SEM). Based on the *in situ* X-ray diffraction data a nucleation mechanism is proposed where an amorphous precursor consisting of clusters with a mix of edge- and corner-sharing NbO_6 octahedra undergo a gradual restructuring to more corner-sharing octahedra, before an abrupt crystallization. For the first time, the Sr fraction in SBN was successfully tuned with the hydrothermal method, both by changing the Sr fraction in the precursor solutions, and by changing the dielectric constant of the solvent. The morphology of SBN was successfully controlled by the synthesis temperature, where low temperatures (175 °C) resulted in rod-shaped particles (length ~1.5 μm and ~500 x 500 nm^2 cross section), and higher temperatures (300 °C) gave cube-shaped particles (~500 x 500 nm^2).

Introduction

Ferroelectric materials are an essential part of our technological society. In later years, there has been an increased interest in nanostructured [1], and especially one-dimensional (1D) nanostructured ferroelectric materials [2, 3]. These 1D materials are important for further development of e.g. non-volatile ferroelectric random-access memories (FeRAM), sensors and/or actuators in microelectromechanical systems (MEMS), nanosized energy-harvesting devices and for fundamental research on finite-size effects on ferroelectric properties [2, 3]. Cheap, controllable, reproducible and environmentally friendly synthesis routes are needed for these applications. Wet chemical methods [4], and especially hydrothermal synthesis stands out as one of the most promising ways of producing 1D nanostructured ferroelectric materials [2, 5].

$Sr_xBa_{1-x}Nb_2O_6$ (x = 0.32 - 0.82, SBN) is a lead-free ferroelectric material with an unfilled tetragonal tungsten bronze (TTB) structure [6-8]. SBN can be tuned from normal to relaxor ferroelectric behaviour by varying the Sr fraction [9] and the Curie temperature (T_c) depends linearly on the Sr fraction and ranges from 60 to 230 °C [10]. In addition SBN has good pyroelectric [11, 12] and photorefractive properties [13]. Moreover, reduced SBN ($Sr_xBa_{1-x}Nb_2O_{6-\delta}$) is reported to have promising thermoelectric properties [14] and filled SBN ($Sr_xBa_{1.2-x}Nb_2O_6$) is reported to show low temperature superconductivity [15].The crystal structure of SBN consists of corner-sharing NbO_6 octahedra forming triangular C-sites (empty in SBN), square A1-sites and pentagonal A2-sites [6, 16] filled with a total of 5 alkaline earth atoms, and 1 vacancy, as shown in Figure 1. The average structure is described by the *P4bm* space group, but a better understanding of the link between order/disorder, polarization and incommensurate tilting of NbO_6 octahedra in the structure is still being addressed [16, 17]. The three species, ((5-x)*Sr^{2+}, x*Ba^{2+} and one vacancy) are distributed on a total of 6 sites per unit cell (2 A1- and 4 A2-sites), and one X-ray diffraction experiment is not sufficient to determine the occupancy of Ba^{2+}, Sr^{2+} and the vacancy on the two sites due to parameter correlations [18]. Therefore, it is often assumed that the larger Ba^{2+} can only occupy the larger A2-site, while Sr^{2+} can occupy both the A1- and A2-sites when doing Rietveld refinements [6, 19, 20], but recently the possibility for cation vacancy disorder have been addressed with simulations [21, 22] and experimentally [23].

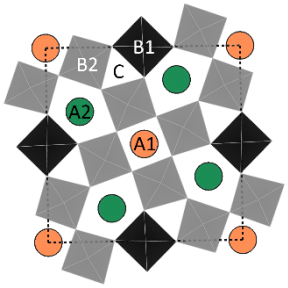

Figure 1. Crystal structure of SBN seen along the *c* axis of the tetragonal cell. NbO_6 octahedra are indicated in black and grey (B1 and B2), the square A1 sites are orange, the pentagonal A2 sites are green and the triangular C sites are empty.

[a] *Department of Materials Science and Engineering, NTNU Norwegian University of Science and Technology, 7491 Trondheim, Norway.*
[b] *Swiss-Norwegian Beamlines at European Synchrotron Research Facility, 38043 Grenoble, France.*

Electronic Supplementary Information (ESI) available: Figures showing selected temperature profiles. Typical input file and more details for the batch Rietveld refinement and representative fits. Validation of the Rietveld refinement model. Details about TEM study. SEM images of all experiments. Summary of all refined values at the end of the experiments. Effect of alkaline earth to niobium ratio on Rietveld refinements. See DOI: 10.1039/x0xx00000x

One vacancy per unit cell, which is distributed on the A1- and A2-site is not shown. Figure made using VESTA [24].

Several methods have been used to prepare SBN [25], where large single crystal SBN made with the Czochralski technique is the most common for utilizing the optical properties of SBN [7, 9, 26]. SBN is also routinely made by solid-state synthesis using $BaCO_3$ or $Ba(NO_3)_2$, $SrCO_3$ and Nb_2O_5 and calcining at temperatures from 1200 to 1400 °C [10, 19, 23]. Other synthesis routes are also described, like combustion synthesis [27], molten salt synthesis [28], urea method [29] and hydrothermal synthesis [30]. All these methods have one or several of the following drawbacks; high temperature, slow, involve the use of hydrofluoric acid in precursor preparation, or issues with reproducibility.

In this work, we present a new hydrothermal route for producing SBN studied with in situ synchrotron X-ray diffraction. The in situ experiments allow optimizing of synthesis parameters, such as reaction temperature and Sr fraction in precursor, to suppress the formation of secondary phases. It is demonstrated for the first time that the composition (ratio between Sr and Ba) of SBN can be controlled with the hydrothermal method, and both rod-, tube-, and cube-shaped particles were obtained for different reaction conditions.

Experimental

Synthesis

Nominal composition $Sr_xBa_{1-x}Nb_2O_6$ (x = 0.2 – 0.6) was prepared from strontium nitrate (Sigma-Aldrich, Oslo, Norway, 99.995 %), barium nitrate (Sigma-Aldrich, Oslo, Norway, 99.999 %) and niobium acid. The niobium acid was prepared by dissolving approximately 70 g of ammonium niobate (V) oxalate hydrate (Sigma-Aldrich, Oslo, Norway, 99.99 %) in 700 mL distilled water under continuous stirring at 50 °C for 3-5 h until a clear solution was obtained. Then the pH was increased to 11 with addition of aqueous ammonia solution (Sigma-Aldrich, Oslo, Norway, 25 wt% solution) to precipitate niobium acid, forming a milky white dispersion/slurry. This mixture was stirred at room temperature (RT) for several days. The dispersion was centrifuged (11300 g/10 000 rpm for 15 min) and the collected precipitates were re-dispersed in 1 wt% ammonia solution. This centrifugation procedure was repeated 3 times to remove oxalate ions. After the final centrifugation the precipitate was collected and re-dispersed in 125 mL 1 wt% ammonia solution, giving a final dispersion with pH 11. The niobium content of the niobium acid was standardized using thermogravimetric analysis at 800 °C. For each experiment, 5 mL of precursor was prepared by first weighing out niobium acid giving a final Nb-concentration of 0.25 M. The pH was adjusted to 12.4 with 25 wt% ammonia solution (around 1.5 mL added), before dissolving the stoichiometric amounts of strontium and barium nitrates (amounts varies with x). Finally, distilled water was added to give a total volume of 5 mL. An overview of the synthesis parameters for the experiments conducted are presented in Table 1.

Table 1. Overview of experiment names, temperature, pressure, X-ray wavelength, time resolution and approximate experiment time for the in situ X-ray diffraction experiments. Also, indicated is the final product.

Name [a]	Temperature [°C]	Pressure [bar]	Wavelength [b] [Å]	Time Resolution [c] [s]	Approx. total time of experiment [h]	Final Product
SBN60_T300	300	200	0.77624	5	0.9	SBN, Pyro
SBN60_T225	225	200	0.77624	5	2.3	SBN, Pyro, Uknw
SBN60_T200	200	200	0.77445	5	3.7	SBN, Pyro
SBN50_T400	400	200	0.77624	5	1.3	SBN, Pyro
SBN50_T300	300	200	0.77624	5	0.7	SBN, Pyro
SBN50_T225	225	200	0.77624	5	2.1	SBN, Pyro, Uknw
SBN50_T200	200	200	0.77624	5	3.6	SBN, Uknw
SBN50_T175	175	200	0.77624	10	10.4	SBN, Uknw
SBN40_T300	300	200	0.77624	5	0.6	SBN
SBN40_T225	225	200	0.77624	5	1.3	SBN
SBN40_T200	200	200	0.77445	5	2.4	SBN
SBN30_T300	300	200	0.77445	5	0.6	SBN
SBN30_T225	225	200	0.77445	5	1.4	SBN
SBN30_T200	200	200	0.77445	5	2.6	SBN
SBN20_T300	300	200	0.77445	5	0.5	SBN
SBN20_T225	225	200	0.77445	5	2.2	SBN
SBN20_T200	200	200	0.77445	5	4.1	SBN
SBN50_supercrit	400	250	0.77624	2	3.0	SBN, Uknw

[a] The nomenclature is SBNXX_TYYY, where XX refers to the Sr mole fraction in the precursor times 100 and YYY the reaction temperature. [b] Experiments were conducted at two different beam times, therefore, different wavelengths. [c] Exposure time for each 2D frame for the experiment. Exposure time was optimized for the different reaction rates.

Characterization

In situ X-ray diffraction experiments were performed at two different beam times at the Swiss-Norwegian Beamlines (BM01), European Synchrotron and Radiation Facility (ESRF),

Grenoble, France. The experiments were conducted in transmission mode, using the PILATUS@SNBL platform [31]. The experimental setup is described elsewhere [32-34]. In short, the setup consists of a single crystal sapphire capillary (1.15 ± 0.1 mm outer and 0.8 ± 0.08 mm inner diameter, Crytur, Turnov, Czech Republic) which is pressurized with a high-pressure liquid chromatography (HPLC) pump (Shimadzu LC-10ADVP, Shimadzu Corporation, Kyoto, Japan). Heating was done with a high (max ~750 °C) temperature heat blower (Leister LE Mini 800, Kaegiswil, Switzerland) with nitrogen flow. The heat blower was heated to the desired set-point temperature while directed away from the capillary before being moved into position by a step motor. The set point temperature was reached within ~20 s. Heating profiles at selected temperatures are presented in Figure S1 in the Electronic Supplementary Information (ESI), with a description of the temperature calibration. The precursor slurry was injected into the capillary using a plastic syringe. All experiments were run until no more changes were observed in the diffraction patterns (in intensity and/or peak width).

All raw data frames were masked for parasitic regions (to remove shadow of beam stop and diffraction spots from the single crystal capillary) and integrated from 2D images to 1D diffractograms using *Bubble* (version 2017.10.23) [31]. The sequential batch refinements were performed using *TOPAS* (Bruker AXS version 5) in launch mode, with *jEdit* (version 4.3.1) as the text editor for writing macros for *TOPAS* [35]. The instrumental broadening was calibrated using a NIST 660a LaB_6 standard, fitted with the modified Thompson-Cox-Hastings pseudo-Voigt peak shape [36] provided within *TOPAS*. A typical starting model (input-file in *TOPAS*) and a detailed description of the model used for the refinements is shown in the ESI, in addition to a typical graphical representation of a Rietveld refinement in Figure S2. To validate the refined values for the Sr fraction, a reference using a data set of SBN made by solid-state synthesis provided by Aamlid et al. was used [23]. A full description of this calibration is presented in the ESI, with the Rietveld refinement profiles in Figure S3. In short, the results show that extracted lattice parameters follows what is expected for the given nominal compositions, and that the extracted Sr fractions show the expected trend, but the nominal Sr fraction is underestimated. The nominal Sr fraction is more underestimated for high Sr fractions, as seen in Figure S4. Based on this, the Sr fractions presented in this work can be used to show relative differences between the experiments but are not considered to reflect the true Sr fractions. In this work it is assumed that stoichiometric SBN is formed during the hydrothermal synthesis ($Sr_xBa_{1-x}Nb_2O_6$), and not a filled or reduced version. This has not been verified, and the possibility for non-stoichiometry is briefly discussed.

After the *in situ* diffraction experiments, the samples were collected for *ex situ* scanning electron microscopy (SEM) imaging. An in-lens cold field emission S(T)EM Hitachi S-5500 with an acceleration voltage of 7 keV was used, and secondary electrons were detected. The samples were prepared by dropping a diluted aqueous dispersion of the collected samples onto an aluminium sample holder, which was then dried for 6-7 h at RT. The nature of the experimental setup makes it impossible to separate completely SBN from the precursor, so both unreacted amorphous precursor and crystalline products were observed.

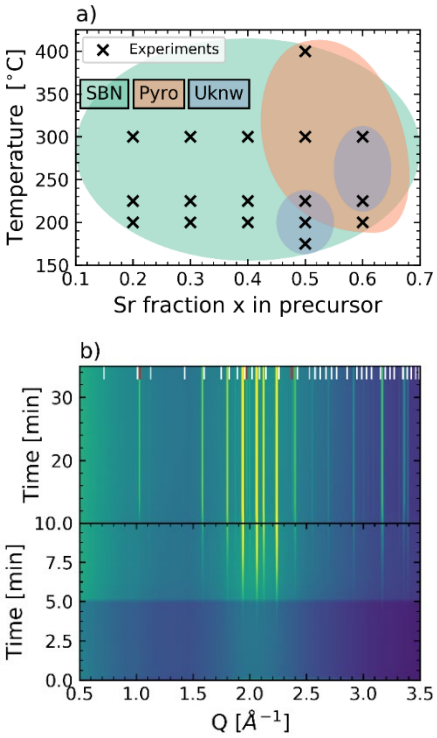

Figure 2. "Phase formation diagram" as a function Sr fraction x in precursor and temperature (a), with crosses indicating experiments in this work. Phase pure SBN is indicated with green (9 experiments), mixture of SBN and Pyro with orange (3 experiments) and mixture of SBN and Uknw with blue (2 experiments). The overlapping green, orange and blue indicates a mix of SBN, Pyro and Uknw (3 experiments). Contour plot (b) of SBN50_T300 showing formation of SBN and Pyro from an amorphous precursor without any intermediate phases. White bars shows theoretical hkl values for SBN at RT, and red bars show the three most intense hkl values for Pyro. For this particular experiment, SBN formed after ~3 min and Pyro after ~10 min.

Results

Phase purity and phase development

Phase pure SBN was obtained for all reaction temperatures in case of SBN20, SBN30 and SBN40, as presented in Table 1 and shown in Figure 2 (a). In the case of SBN50 and SBN60, two secondary phases were observed, a pyrochlore phase (referred to as Pyro) and a phase that has not been identified (referred to as Uknw), in addition to SBN. The Pyro phase was shown to be Sr-rich compared to SBN by transmission electron microscopy (TEM, description and experimental details in ESI). A Pawley fit [37] of the diffractogram of the Pyro phase using the cubic space group $Fd\bar{3}m$ gave a lattice parameter of ~10.55 Å, which also was used further in the Rietveld refinements. Here the lattice parameter was refined for the last frame, and then kept fixed for the batch refinement. No space group was found for the Uknw phase and single peak phases with fixed positions were used (positions fixed to refined values from last frame). Satisfactory Rietveld refinement could not be obtained with all phases present and a quantitative analysis was not possible, but the general trends based on the relative intensities are increasing amount of secondary phases with increasing Sr fraction in the precursor and with increasing temperature. In all

experiments where SBN and Pyro were formed, SBN always formed prior to the Pyro phase before the amount of both phases increased and then stabilized. In the experiments where SBN and the Uknw phase were formed, the Uknw phase always formed first before the amount of both phases increased simultaneously before stabilizing. The amounts of neither Pyro nor Uknw phase decreased due to formation of SBN.

Formation of SBN from the amorphous precursor proceeded without crystalline intermediates as shown in Figure 2 (b). The only exception was experiments were the Uknw phase was formed. A temperature dependent incubation period ranging from a few minutes at high temperatures to ~2 h at the lowest temperature is observed before crystallization in all experiments. After the incubation period the formation and growth of SBN was seemingly fast. This is based on attempts on refining crystallite sizes on the first frames right after SBN formation giving values in the range 50 – 100 nm (indicating rapid growth).

Reaction kinetics

The Johnson-Mehl-Avrami (JMA) equation , Equation 1, was derived for modelling the kinetics of solid state reactions [38], but has also been utilized for kinetic studies of hydrothermal reactions [39-41]. In the JMA equation *f* is the fractional extent of the reaction as a function time (*t*) after the first appearance of the phase, *k* is a rate constant and *n* is an exponent linked to the growth mechanism [38]. Plotting *ln(k)* against the inverse of temperature gives a straight line (assuming the model describes the reaction sufficiently well) with a slope that gives the activation energy of the reaction.

$$f = 1 - \exp(-kt^n) \qquad 1$$

In Figure 3 (a), *ln(k)* is plotted as a function of inverse temperature, and *n* values are presented in Figure 3 (b). The values (*k* and *n*) are obtained by fitting the JMA equation to the time resolved normalized scale factors, which can be used as a measure of the extent of the reaction (*f*) [42]. The *ln(k)* values are clustered together, but they are not forming straight lines for the individual sets of experiments (SBN20, SBN30 etc.), thus activation energies were not possible to extract, and the origin of this is hypothesized in the discussion section. The *n*-values are between 2 and 3.5 indicating a nucleation- and growth controlled-mechanism for all conditions investigated in this work, providing valuable insight to the growth mechanism of SBN under hydrothermal conditions.

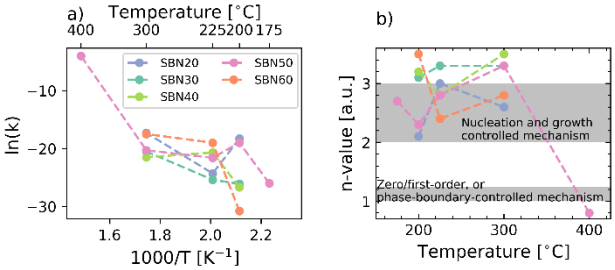

Figure 3. Arrhenius plot (a) and *n*-values (b) obtained from fitting the JMA-equation to the time resolved normalized scale factors.

Crystal structure information from Rietveld refinement

The refined Sr fraction in SBN at the end of the experiments are presented in Figure 4 as a function of reaction temperature and Sr fraction x in the precursor. No clear trends were observed as a function of temperature, although a small decrease in Sr fraction with increasing temperature can be recognized. For all temperatures and Sr fraction in the precursors, the refined Sr fraction is found to be around 0.35 ± 0.1, except for SBN50_supercrit, which stands out with a Sr fraction x from refinement of 0.6. With increasing Sr fraction in the precursors, a close to linear increase in the refined Sr fraction is observed for Sr fractions of 0.2 to 0.5, followed by a decrease going from 0.5 to 0.6. The linear increase is not following a 1:1 relationship between Sr fraction in precursor and Sr fraction from the Rietveld refinement.

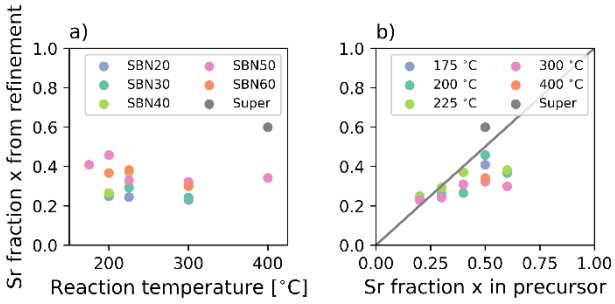

Figure 4. Sr fraction x from Rietveld refinement at the end of the experiments as a function of reaction temperature (a) and Sr fraction x in precursor (b). Gray line in (b) indicates a 1:1 relation between Sr fraction x in precursor and from refinement.

The *a*- and *c*-lattice parameters from the Rietveld refinements at the end of the experiment are plotted against reaction temperature and Sr fraction in the precursor in Figure S6 in the ESI. No clear overall trend as a function of reaction temperature is observed. A minor decrease in *a*, and a small increase in *c* as a function of temperature is observed for each data set. The refined *a* lattice parameters increases while *c* is decreasing as a function of Sr fraction in the precursor in the range 0.2 to 0.5.

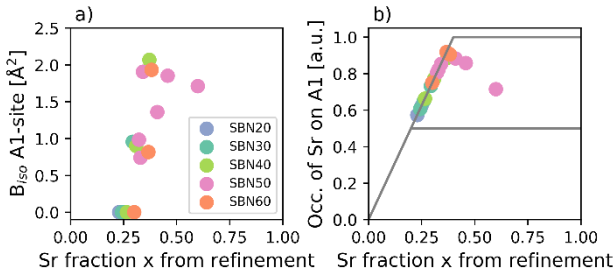

Figure 5. B_{iso} for the A1-site (a) and fractional occupancy of Sr on the A1-site (b) as a function of Sr fraction from the Rietveld refinement. Grey lines shows the minimum and maximum occupancy of Sr on the A1-site given the Rietveld refinement. For Sr fraction lower the 0.2, the minimum and maximum Sr occupancy on the A1-site are identical since Ba is occupying all A2-sites (follows from the assumption that Sr + Ba = 5, and all Ba is locked to the A2-site).

Disorder and/or non-stoichiometry

Nonphysical atomic displacement parameters (ADP, B_{iso}-values equal to 0) for the A1-site resulted from refinements for some of the experiments as presented in Figure 5 (a), where the B_{iso} of the A1-site is plotted against the Sr fraction. The B_{iso} value for the A1-site was constrained to be positive or 0 during the refinements. If the B_{iso} value was refined without this

constraint, the value would return negative for the cases where the B_{iso} now equals 0. The nonphysical B_{iso} values only occur for the experiments with the lowest refined Sr fractions. The fractional occupancy of Sr on the A1-site is presented in Figure 5 (b). The Sr occupancy on the A1-site is perfectly linear and follows the upper limit for Sr occupancy as restricted by the Rietveld refinement up to a Sr fraction of ~0.4. All refined parameters and R-values for the end of all experiments in this work are presented in Table S2 in ESI.

Size and morphology of SBN

SEM images of SBN50 at different reaction temperatures are presented in Figure 6. Rod shaped particles with a length of ~1.5 μm and a ~500 x 500 nm^2 cross section is observed for SBN50_T175. With increasing temperature, the aspect ratio decreases, and for SBN50_T300, SBN50_T400 and SBN50_supercrit only cube shaped SBN is observed (~500 x 500 nm^2). A decrease in aspect ratio with increasing reaction temperature is also observed for the other compositions except for SBN20, as seen in Figure S7 in ESI. In Figure 7, SEM images of SBN formed at 300 °C and varying Sr fraction are presented. Here, cube shaped SBN with similar size (500 x 500 nm^2) is observed for all Sr fractions except for SBN20_T300. For SBN20_T300 tubes with a rectangular cross section are observed.

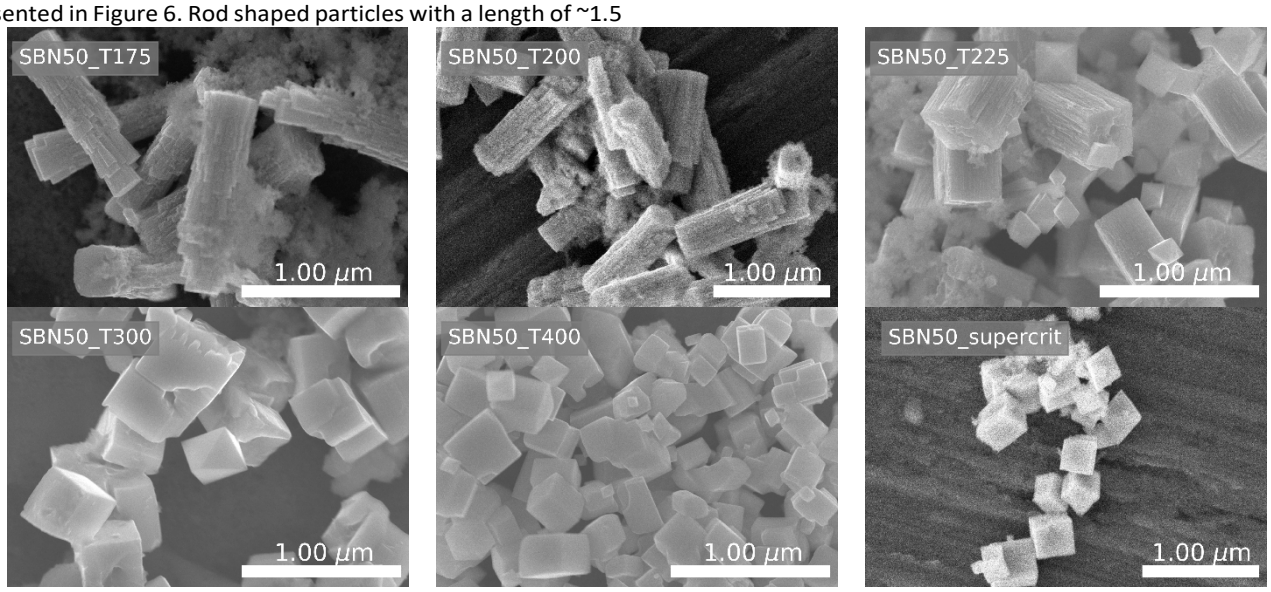

Figure 6. SEM images of SBN particles made with a Sr fraction x in the precursor of 0.5 at different reaction temperatures, SBN50_T175, SBN50_T200, SBN50_T225, SBN50_T300, SBN50_T400 and SBN50_supercrit.

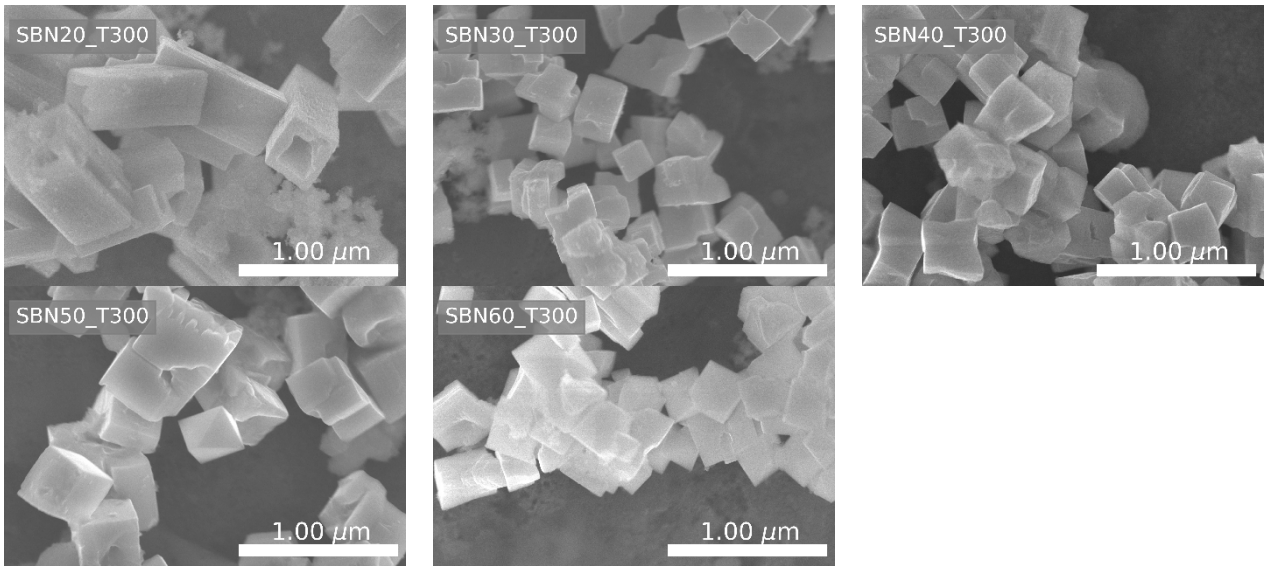

Figure 7. SEM images of SBN particles made with a reaction temperature of 300 °C with different Sr fraction x in the precursor, SBN20_T300, SBN30_T300, SBN40_T300, SBN50_T300 and SBN60_T300.

In some of the SEM images smaller bipyramids are observed (especially visible in SBN60_T300 and SBN50_T225), which is the Pyro phase. The Pyro phase forming bipyramids was determined by TEM (see ESI). No features in the SEM images could be ascribed to the Uknw phase. From the *in situ* diffraction experiments the Uknw phase appeared as strong spots on the detector (not full diffraction cones on the 2D

detector, which indicates large and few crystallites), which can explain why it has not been found in the SEM images.

Discussion

Phase pure SBN particles were successfully synthesized with the new hydrothermal route presented in this work. The work demonstrates that the morphology of SBN can be modified by varying the reaction temperature, and that the composition of the final SBN can be tuned with the Sr fraction in the precursor and the dielectric constant of the solvent, through changes in temperature and pressure.

Nucleation and growth of SBN

The time-dependent X-ray diffraction results show that a temperature dependent incubation period is needed before the nucleation of SBN occurs, and that the first observed crystallites are relatively large (~50 nm) and hence the growth rate is fast. Similar characteristics have been reported for the formation of WO_3 under hydrothermal conditions by Saha *et al.* [43]. WO_3 , with the archetype *P6/mmm* crystal structure for tungsten bronzes (TB), has a crystal structure strongly related to SBN. Amorphous precursor consists of clusters with a mix of corner- and edge-sharing WO_6 octahedra was demonstrated by *in situ* X-ray total scattering with Pair Distribution Function (PDF) analysis. When heat was applied, a gradual decrease in the signature of the edge-sharing octahedra was observed with a simultaneous increase in the signature of the corner-sharing octahedra, which is the only building block in TB. Once most octahedra are corner-sharing an abrupt formation of crystalline particles were observed. Based on the results presented in this work, and the similarities with the work of Saha *et al*. a related formation mechanism is proposed for SBN under hydrothermal conditions, schematically illustrated in Figure 8. The precursor consists of clusters with corner and edge sharing NbO_6 octahedra and alkaline earth ions in solution. With increasing temperature, a gradual reorientation of the octahedra occurs, before abrupt crystallization. With increasing degree of corner-sharing octahedra, the Nb-O network gets increasingly negatively charged (fewer shared oxygen), thus increasing the driving force for the alkaline earth ions to enter the clusters/structure by the need for charge compensation. Sr^{2+} and Ba^{2+} ions are thus proposed to enter the clusters during the reorientation of the octahedra. A similar formation scheme have also been proposed for $K_xNa_{1-x}NbO_3$ (KNN) under hydrothermal conditions, but then with a crystalline intermediate with edge-sharing NbO_6 octahedra transforming into the corner-sharing perovskite structure of KNN [44]. The proposed formation mechanism for SBN has not been verified by X-ray total scattering and PDF analysis as in the case of WO_3.

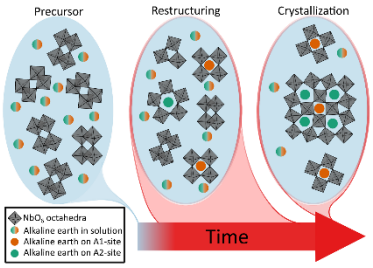

Figure 8. Proposed reaction scheme for the nucleation of SBN. Initially the amorphous precursor consists of clusters with a mix of edge- and corner-sharing NbO_6 octahedra. With heat, the clusters undergo a continuous and gradual restructuring to more corner-sharing octahedra, before an abrupt crystallization occurs. Alkaline earth ions are believed to enter the clusters/structure continuously during this process.

After the nucleation of SBN the growth rate is fast. The final shape of the particles is cubes with dimensions ~500 x 500 x 500 nm^3 at higher temperatures (SBN50_T300) and rods ~1.5 μm long with a ~500 x 500 nm^2 cross section at lower temperatures (SBN50_T175). Here we propose that the lower nucleation rate at lower temperatures leads to the formation of relatively few crystallites, that combined with a longer reaction time, will give good conditions for growth into the most favourable morphology for SBN. Hydrothermally synthesized SBN have been reported to form rods [30], and from solid-state synthesis of SBN abnormal grain growth is known, leading to large anisometric grains [25]. In addition, the anisometric unit cell is likely to promote 1D growth, which for example is the case of the tungsten oxide $K_{0.4}WO_3$ forming long whiskers under hydrothermal synthesis [45] and the proposed Wulff construction of WO_3 having the shape of hexagonal rods [46]. The rod-shaped particles at lower temperatures are therefore assumed to be the preferred shape, or Wulff construction, of SBN, growing by monomer/cluster addition in its preferred direction (*c*-direction). With increasing temperature, the nucleation rate increases, leading to a faster depletion of precursor and a shorter reaction time. This hinders SBN from reaching its preferred shape of rods, giving cubes with a similar cross section as the rods. For even higher temperatures a small decrease in the size of the SBN cubes is observed, which is also linked to the higher nucleation rate and faster depletion of precursor, and thus less growth. This is further supported by the reported *n*-values, showing a nucleation- and growth-controlled mechanism. A more thorough parameter study on what governs the formation of rods, cubes and tubes is in progress.

The different sizes, morphologies and secondary phases forming throughout the experiments presented here are likely to explain why the Arrhenius plots does not show straight lines, and no activation energies can be obtained. The JMA-model assumes among other things growth of spherical particles, which is not the case in the current work.

Sr fraction and microstructure from Rietveld refinement

The Sr fraction in SBN increases close to linearly with Sr fraction in the precursor in the range from 0.2 to 0.5, with a drop in Sr fraction from 0.5 to 0.6. The linear increase is expected, and the drop between 0.5 to 0.6 is explained with the increasing amount of the Sr-rich Pyro phase at higher Sr fraction. The linear increase is not 1:1, which can be an effect of the different

solubility of $Ba(NO_3)_2$ and $Sr(NO_3)_2$ [47], where $Sr(NO_3)_2$ is more soluble in water and therefore to a larger degree stays in solution. It can also be an artefact of the model used for the Rietveld refinements, where we showed with the reference on the solid-state synthesis samples that the Sr fraction is underestimated, especially at higher Sr fractions.

The experiment SBN50_supercrit gave a higher Sr fraction of 0.6 from the Rietveld refinement compared the other experiments (around 0.35 ± 0.1). As water becomes supercritical, the dielectric constant drops significantly and changes the solvent properties [5]. Both $Ba(NO_3)_2$ and $Sr(NO_3)_2$ are only slightly soluble in ethanol at RT [47], which has a comparable dielectric constant to water at 400 °C and 250 bar (supercritical conditions). Thus, the solubility of both $Ba(NO_3)_2$ and $Sr(NO_3)_2$ will be close to zero for SBN50_supercrit. The smaller Sr^{2+} can easier enter the SBN structure, explaining why the increased Sr fraction is observed at supercritical conditions. To fully control the Sr fraction without introducing secondary phases, changing the dielectric constant of the solvent, either by going supercritical or having a mixed solvent, looks promising based on the present work.

In literature it is reported that both the *a* and *c* parameters decrease with increasing Sr fraction at RT [20]. The *c* parameter in this work is thus following the expected trend with respect to both Sr fraction in precursor and Sr fraction from refinement, while *a* shows the opposite trend. No good explanations are found for this discrepancy other than the possibility of incorporation of hydroxyl groups in the structure. Hydroxyl groups have been shown to lay perpendicular to the *c*-axis in the SBN structure [48, 49], thus influencing the *a* parameter more than the *c* parameter.

Disorder and/or non-stoichiometry

B_{iso} values equal to 0 (negative if not constrained in the refinement) for the A1 site indicates a too low electron density on this site. Similarly, the Sr occupancy on the A1 site strictly following the upper limit for low Sr fractions also seems to indicate that the Rietveld refinement algorithm is trying to maximize the electron density on the A1 site by increasing the Sr occupancy on the A1-site. The too low electron density on the A1 site might show that the real system contains some degree of disorder, for example Ba on the A1 site, which is not accounted for by the model used or that the total amount of Sr and Ba is actually higher than 5. To check this hypothesis the last frame of SBN30_T300 was refined with varying total amounts of Sr and Ba, see ESI for a full description. These results points towards better overall fits and more physically sound values when increasing the total amount of Sr and Ba. A similar investigation was done for the effect of disorder by placing some Ba on the A1-site. With increasing amount of Ba on the A1-site, the overall fits became better, and more physically sound values were obtained. These results do not provide enough evidence with respect to disorder vs. non-stoichiometry but highlights the complexity of SBN, and that our Rietveld refinement model is not capturing all features of SBN synthesized under the hydrothermal conditions used in this work.

Conclusion

A hydrothermal synthesis route for SBN was developed, enabled by a thorough *in situ* X-ray diffraction investigation. A formation mechanism for SBN is proposed, where the precursor consist of clusters of corner- and edge-sharing octahedra that gradually restructure into more corner-sharing clusters, before an abrupt crystallization. We have for the first time tuned the Sr fraction in SBN (from 0.25 to 0.6) by hydrothermal synthesis, both by changing the Sr fraction x in the precursor, and by changing the dielectric constant of the solvent. Tuning the Sr fraction under synthesis has a great potential since the Sr content is important for tailoring the properties of SBN. Furthermore, it is shown how the size and morphology of the SBN particles can be controlled by the reaction temperature and/or Sr fraction in precursor, with rod-, tube- and cube-shaped particles observed. Based on the morphologies observed, a possible growth mechanism is described.

Conflicts of interest

There are no conflicts to declare.

Acknowledgements

MSc. Solveig Stubmo Aamlid is acknowledged for fruitful discussions on the Rietveld refinements of SBN. Financial support from NTNU Norwegian University of Science and Technology and The Research Council of Norway under the Toppforsk program to the project (No 250403) “From Aqueous Solutions to oxide Thin films and hierarchical Structures” is gratefully acknowledged. The Research Council of Norway is acknowledged for the support to NTNU NanoLab through the Norwegian Micro and Nano-Fabrication Facility, NorFab, project number 245936/F50 and the Norwegian Center for Transmission Electron Microscopy, NORTEM (197405/F50). We are grateful to the Swiss-Norwegian Beamlines (SNBL) BM01 at European Synchrotron Radiation Facility (ESRF, Grenoble, France) for granting access time to CRG beam times.

References

1. J. Varghese, R. W. Whatmore and J. D. Holmes, *J. Mater. Chem. C*, 2013, **1**, 2618-2638.
2. P. M. Rørvik, T. Grande and M.-A. Einarsrud, *Adv. Mater.*, 2011, **23**, 4007-4034.
3. L. Liang, X. Kang, Y. Sang and H. Liu, *Adv. Sci.*, 2016, **3**, 1500358-n/a.
4. M. E. Villafuerte-Castrejon, E. Moran, A. Reyes-Montero, R. Vivar-Ocampo, J. A. Pena-Jimenez, S. O. Rea-Lopez and L. Pardo, *Materials*, 2016, **9**, 27.
5. M.-A. Einarsrud and T. Grande, *Chem. Soc. Rev.*, 2014, **43**, 2187-2199.
6. P. B. Jamieson, S. C. Abrahams and J. L. Bernstein, *J. Chem. Phys.*, 1968, **48**, 5048-5057.
7. M. Ulex, R. Pankrath and K. Betzler, *J. Cryst. Growth.*, 2004, **271**, 128-133.

8. X. Zhu, M. Fu, M. C. Stennett, P. M. Vilarinho, I. Levin, C. A. Randall, J. Gardner, F. D. Morrison and I. M. Reaney, *Chem. Mater.*, 2015, **27**, 3250-3261.
9. T. Lukasiewicz, M. A. Swirkowicz, J. Dec, W. Hofman and W. Szyrski, *J. Cryst. Growth.*, 2008, **310**, 1464-1469.
10. J. Zhang, G. Wang, F. Gao, C. Mao, F. Cao and X. Dong, *Ceram. Int.*, 2013, **39**, 1971-1976.
11. A. M. Glass, *J. Appl. Phys.*, 1969, **40**, 4699-4713.
12. H. Tang, X.-G. Tang, M.-D. Li, Q.-X. Liu and Y.-P. Jiang, *J. Alloy. Compd.*, 2019, **791**, 1038-1045.
13. M. D. Ewbank, R. R. Neurgaonkar, W. K. Cory and J. Feinberg, *J. Appl. Phys.*, 1987, **62**, 374-380.
14. S. Lee, R. H. T. Wilke, S. Trolier-McKinstry, S. Zhang and C. A. Randall, *Appl. Phys. Lett.*, 2010, **96**, 031910.
15. T. Kolodiazhnyi, H. Sakurai, M. Isobe, Y. Matsushita, S. Forbes, Y. Mozharivskyj, T. J. S. Munsie, G. M. Luke, M. Gurak and D. R. Clarke, *Phys. Rev. B*, 2015, **92**, 214508.
16. M. Paściak, P. Ondrejkovic, J. Kulda, P. Vaněk, J. Drahokoupil, G. Steciuk, L. Palatinus, T. R. Welberry, H. E. Fischer, J. Hlinka and E. Buixaderas, *Phys. Rev. B*, 2019, **99**, 104102.
17. P. Y. Vanina, S. B. Vakhrushev, A. A. Naberezhnov and A. A. Bosak, *Journal of Physics: Condensed Matter*, 2019, **31**, 175401.
18. C. Heremans, B. J. Wuensch, J. K. Stalick and E. Prince, *J. Solid State Chem.*, 1995, **117**, 108-121.
19. J. G. Carrio, Y. P. Mascarenhas, W. Yelon, I. A. Santos, D. Garcia and J. A. Eiras, *Mater. Res.*, 2002, **5**, 57-62.
20. S. Podlozhenov, H. A. Graetsch, J. Schneider, M. Ulex, M. Wohlecke and K. Betzler, *Acta Crystallogr. Sect. B*, 2006, **62**, 960-965.
21. G. H. Olsen, S. M. Selbach and T. Grande, *Phys. Chem. Chem. Phys.*, 2015, **17**, 30343-30351.
22. G. H. Olsen, U. Aschauer, N. A. Spaldin, S. M. Selbach and T. Grande, *Phys. Rev. B*, 2016, **93**, 180101.
23. S. S. Aamlid, M. S. Selbach and T. Grande, *Materials*, 2019, **12**.
24. K. Momma and F. Izumi, *J. Appl. Crystallogr.*, 2011, **44**, 1272-1276.
25. A. R. Kulkarni and P. K. Patro, *Trans. Indian Cer. Soc.*, 2010, **69**, 135-146.
26. J. Schefer, D. Schaniel, V. Petříček, T. Woike, A. Cousson and M. Wöhlecke, *Z. Kristallogr. Cryst. Mater.*, 2008, **223**, 399.
27. P. K. Patro, A. R. Kulkarni and C. S. Harendranath, *Mater. Res. Bull.*, 2003, **38**, 249-259.
28. C. Duran, G. L. Messing and S. Trolier-McKinstry, *Mater. Res. Bull.*, 2004, **39**, 1679-1689.
29. G.-h. Chen, J.-t. Liu, H.-r. Xu, C.-r. Zhou, M.-h. Jiang and X.-y. Liu, *J. Mater. Sci.: Mater. Electron.*, 2011, **22**, 915-919.
30. A. Xia, Q. Ding, H.-y. Miao and G.-q. TAN, *Elec. Comp. Mat.*, 2007, **26**, 37.
31. V. Dyadkin, P. Pattison, V. Dmitriev and D. Chernyshov, *J Synchrotron Radiat*, 2016, **23**, 825-829.
32. J. Becker, M. Bremholm, C. Tyrsted, B. Pauw, K. M. O. Jensen, J. Eltzholt, M. Christensen and B. B. Iversen, *J. Appl. Crystallogr.*, 2010, **43**, 729-736.
33. S. L. Skjærvø, K. H. Wells, S. Sommer, T.-D. Vu, J. R. Tolchard, W. van Beek, T. Grande, B. B. Iversen and M.-A. Einarsrud, *Cryst. Growth Des.*, 2018, **18**, 770-774.
34. A. R. M. Dalod, O. G. Grendal, S. L. Skjærvø, K. Inzani, S. M. Selbach, L. Henriksen, W. van Beek, T. Grande and M.-A. Einarsrud, *J. Phys. Chem. C*, 2017, **121**, 11897-11906.
35. J. S. O. Evans, *Mater. Sci. Forum*, 2010, **650**, 1-9.
36. P. Thompson, D. E. Cox and J. B. Hastings, *J. Appl. Crystallogr.*, 1987, **20**, 79-83.
37. G. Pawley, *J. Appl. Crystallogr.*, 1981, **14**, 357-361.
38. M. Avrami, *J. Chem. Phys.*, 1939, **7**, 1103-1112.
39. P. Nørby, M. Roelsgaard, M. Søndergaard and B. B. Iversen, *Cryst. Growth Des.*, 2016, **16**, 834-841.
40. H. L. Andersen, K. M. Ø. Jensen, C. Tyrsted, E. D. Bøjesen and M. Christensen, *Cryst. Growth Des.*, 2014, **14**, 1307-1313.
41. J. R. Eltzholtz, C. Tyrsted, K. M. O. Jensen, M. Bremholm, M. Christensen, J. Becker-Christensen and B. B. Iversen, *Nanoscale*, 2013, **5**, 2372-2378.
42. K. M. Peterson, P. J. Heaney and J. E. Post, *Chem. Geol.*, 2016, **444**, 27-36.
43. D. Saha, K. M. Ø. Jensen, C. Tyrsted, E. D. Bøjesen, A. H. Mamakhel, A.-C. Dippel, M. Christensen and B. B. Iversen, *Angew. Chem. Int. Ed.*, 2014, **53**, 3667-3670.
44. S. L. Skjærvø, K. H. Wells, W. van Beek, T. Grande and M.-A. Einarsrud, *CrystEngComm*, 2018, **20**, 6795-6802.
45. X.-G. Yang, C. Li, M.-S. Mo, J.-h. Zhan, W.-C. Yu, Y. Yan and Y.-T. Qian, *J. Cryst. Growth.*, 2003, **249**, 594-599.
46. T. Lee, Y. Lee, W. Jang and A. Soon, *J. Mater. Chem. A*, 2016, **4**, 11498-11506.
47. *CRC Handbook of Chemistry and Physiscs, 99th Edition (Internet Version 2018)*, CRC Press/Taylor & Francis, Boca Raton, Florida, USA.
48. S. Hunsche, A. Gröne, G. Greten, S. Kapphan, R. Pankrath and J. Seglins, *Phys. Status Solidi A*, 1995, **148**, 629-634.
49. M. Lee, H. S. Lee and R. S. Feigelson, *J. Appl. Phys.*, 1998, **84**, 1558-1560.

Article